PAPER · OPEN ACCESS

Response of tungsten surfaces to helium and hydrogen plasma exposure under ITER relevant steady state and repetitive transient conditions

To cite this article: L. Buzi *et al* 2017 *Nucl. Fusion* **57** 126009

View the article online for updates and enhancements.

Response of tungsten surfaces to helium and hydrogen plasma exposure under ITER relevant steady state and repetitive transient conditions

L. Buzi[1,2,3,a], G. De Temmerman[4], A.E. Huisman[5], S. Bardin[3], T.W. Morgan[3], M. Rasinski[2], R.A. Pitts[4] and G. Van Oost[1,6]

[1] Department of Applied Physics, Ghent University, Sint-Pietersnieuwstraat 41, B-9000, Ghent, Belgium
[2] Forschungszentrum Jülich, Institut für Energie und Klimaforschung, 52425 Jülich, Germany
[3] DIFFER-Dutch Institute for Fundamental Energy Research, De Zaale 20, 5612 AJ Eindhoven, Netherlands
[4] ITER Organization, Route de Vinon-sur-Verdon, CS90 046, 13067 St Paul Lez Durance Cedex, France
[5] Eindhoven University of Technology, 5612 AZ Eindhoven, Netherlands
[6] National Research Nuclear University 'MEPHI', Moscow, Russian Federation

E-mail: lbuzi@princeton.edu

CrossMark

Abstract

The effect of helium (He) plasma exposure, and associated surface modifications, on the thermal shock resistance of tungsten (W) under ITER relevant steady state and transient heat and particle loads was studied. W samples were exposed to steady state and pulsed He plasmas at surface base temperatures from 670 to 1170 K. The same exposures were repeated in hydrogen (H) to allow a direct comparison of the role of the ion species on the thermal shock resistance. Exposure to He plasma pulses caused the formation of fine cracking network on W samples which occurred at a higher density and smaller depths compared to H pulsed plasma irradiation. The peak temperature reached during an ELM-like plasma pulse increased by a factor ~1.45 over the 100 s of He plasma exposure, indicating a deterioration of the thermal properties. Transient loading experiments were also performed using a high power pulsed laser during He plasma exposure, showing a significant modification of the target thermal response caused by the surface damage. The effect of He-induced morphology changes on the thermal response modification was found to be very small compared to that of transient-induced damage.

Keywords: tungsten, hydrogen, cracking, laser, transients, helium

(Some figures may appear in colour only in the online journal)

[a] Present address: Department of Chemical and Biological Engineering, Princeton University, Princeton, NJ, United States of America.

1. Introduction

Tungsten (W) is the selected plasma-facing material for the ITER divertor due to its favorable thermal and mechanical properties, and its low sputtering yield [1, 2]. However, exposure to energetic particles (up to several hundreds of eV) such as H isotopes (D, T), He and impurities causes surface modifications (i.e. blisters, nano-bubbles, fuzz, cracking etc), which can lead to an increase of the erosion yield, dust formation and deterioration of the thermal and mechanical properties [1–3].

As a consequence of the lower threshold power for access to H-mode confinement, during the early years of operations, He plasmas are currently under consideration for ITER as means to obtain, characterize and test the mitigation of edge localized modes (ELMs) [2]. One of the potential issues associated with this approach is the possibility that He-induced morphology changes may lower the transient damage threshold due, in particular, to sub (melting) threshold ELMs. Similar issues may also be experienced during the D-T operation phases where He is the ash product of the fusion reaction and will therefore be present in the divertor plasma.

He nano-bubble formation in the near surface is in fact the precursor to fuzz formation at high surface temperature [4, 5]. The bubble size and growth rate are closely related to the surface temperature, meaning that the dominating formation mechanism is most probably the trapping of He at thermal vacancies in the material. Nano-bubbles were observed at surface temperature higher than 500 K, particle fluences ~10^{26} He$^+$ m^{-2} and low ion energy [6–8]. Under divertor-relevant conditions, bubble formation proceeds rapidly. A dense network of He bubbles was observed after a single H-mode He discharge in DIII-D [9] in agreement with earlier observations, albeit at higher temperatures, in Pilot-PSI [10]. The ion energies and surface temperature expected during the He phase in ITER are such that bubble formation can be expected over a significant fraction of the high heat flux area of the W divertor [11].

Other works have used plasma guns and laser heating to simulate ITER-like ELMs and have studied several phenomena such as melting, dust generation and surface morphology changes [12–16]. However, in this paper we have conducted a systematic study, addressing the effects of He plasma exposure, and associated surface modifications, on the thermal shock resistance of W under ITER relevant steady state and transient heat and particle loads. ELM-like loading was replicated using the pulsed plasma system in Pilot-PSI [17], and a high power laser. Controlled experiments were performed with H plasma exposures to assess differences in the thermal shock behavior of He and H exposed surfaces.

2. Experimental setup

W samples with properties in accordance with the specification defined by the ITER Organization [18] were cut from the same rod in discs with a diameter of 14 mm and 4 mm thickness, in such a way that the grains were elongated perpendicular to the plasma-exposed surface. The average grain size in the direction parallel to the exposed surface was 40 μm and the grains

Figure 1. Tungsten sample with the TZM clamping ring.

were elongated perpendicularly up to a few hundreds of μm by forging (hammering) the W rods after sintering. Prior to the plasma exposure, samples were mechanically polished to a mirror finish (R_a ~ 20 nm), ultrasonically cleaned in acetone and alcohol to remove the polishing residuals and annealed for 1 h at 1273 K.

Exposures to He and H plasmas were carried out in the Pilot-PSI linear plasma device [17], which uses a cascaded arc source to generate the plasma. The working gas is injected at the source and the plasma beam spreads in a nearly 1 m long vacuum vessel with a neutral background density lower than 0.01 mbar. In these experiments, the required ion fluence was accumulated using consecutive plasma discharges of 10 s in between which about 20 min was allowed between the discharges for the magnets to cool down. To replicate the transient heat and particle loads, the pulsed plasma system of Pilot-PSI was used [17, 19]. In this case, the DC power supply was connected in parallel with a capacitor bank, which transiently increased the input power to the plasma source resulting in the superimposition of a transient high power plasma pulse to the steady-state plasma. This allows the conditions expected during ELMs in tokamaks to be closely simulated, although the particle energies (characteristic of the tokamak H-mode pedestal temperature) cannot be reproduced in Pilot. In the present experiments, the plasma pulse duration was ~1 ms and the temporal shape followed nearly-square waveform with a frequency of 10 Hz. The capacitor bank voltage, which determines the peak heat flux during the ELM-like pulse, was varied in the range 1.2–1.8 kV.

Plasma electron density and temperature were measured using a Thomson scattering setup [20], 17 mm in front of the target. In these experiments, the plasma consisted mainly of singly ionized ions and the ion energy was calculated from the empirical formula $E_{ion} = U_{bias} - 2kT_e$ [21]. An accelerating negative voltage of -50 V was applied on the target; corresponding to ion energy of 40 eV while the influence of the plasma potential was negligible. In ITER however, the particles coming from the pedestal region and are expelled during an ELM, are expected to reach several keV at the targets [22] while the plasma separatrix temperature during H-mode operation will be in the range 200–350 eV [23].
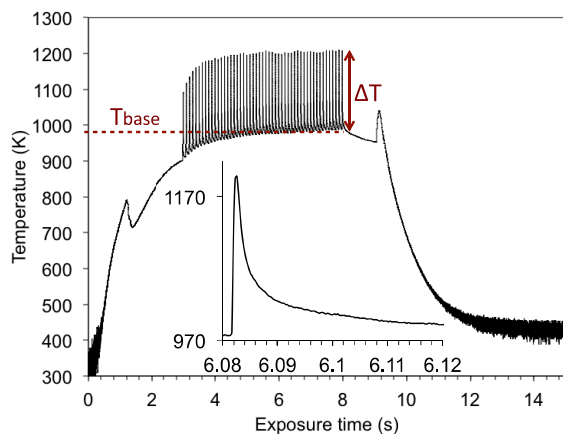
Figure 2. Infrared camera temperature profiles during one plasma discharge in He using the pulsed plasma source at pilot-PSI and a single pulse in plotted in the inserted graph.

During plasma exposure, the W samples were clamped on water-cooled holder (figure 1) and aligned with respect to the peak plasma temperature and density profile, which were nearly homogeneous across the sample diameter (see [17]). Direct 2D measurements of the surface temperature profile were performed with a FLIR SC7500-MB fast infrared (IR) camera with 0.33 mm spatial resolution and a maximum frequency of 30 kHz, providing good temporal resolution for tracking the temperature evolution after an ELM-like heat pulse. The IR camera was calibrated against a black body source. A multi-wavelength pyrometer (FMPI FAR SpectroPyrometer, range 1–1.7 μm, 1.56 nm resolution) was used to cross check the surface temperature *in situ* and provide emission/transmission calibration data for the IR camera [24]. Figure 2 shows an example of the temperature profile recorded with the IR camera during one He plasma discharge.

Plasma heating during the first 3 s of operation set the base temperature and when the plasma pulses were triggered, the temperature increased by a value ΔT_{ELM} (difference between the peak and base temperature) above the base temperature. Heat fluxes deposited on the W samples were calculated from the measured temperature profiles using THEODOR code [25] which numerically solves the heat conduction equation [26]: $\rho C \mathrm{d}T(x,t)/\mathrm{d}t = \nabla(-k\mathrm{d}T(x,t)/\mathrm{d}x)$ with C and k the temperature dependent heat capacity and heat conduction coefficient and $T(x,t)$ is the time dependent measured temperature on the surface. The surface temperature was calculated by considering the temperature dependent emissivity coefficients. The boundary conditions for the heat flux calculations at the top and at the bottom of the sample were defined from the heat transfer coefficients, which had to be optimized [26].

$$q_{\text{plasma}} = \alpha_{\text{top}}(T_{\text{IR}} - T_{\text{bulk}})$$

$$q_{\text{cooling}} = \alpha_{\text{bottom}}(T_{\text{bulk}} - T_{\text{cooling}}).$$

Similar analysis as described in [19] was followed. A value for α_{top} was derived in order to avoid negative heat fluxes after the transients and it is associated with the presence of a thin layer of reduced heat conductivity at the surface while α_{bottom} was derived empirically by reducing the heat flux to zero after the plasma discharge.

Two sets of samples were exposed to pure He and H plasmas under similar plasma exposure conditions, ion energy and surface temperature. The transient heat load density was varied from ~0.2 to ~0.5 MJ m^{-2} and the base surface temperature ranged from ~670 to 1170 K. The total plasma exposure time was ~100 s while the ion fluence reached up to ~7.7 · 10^{25} m^{-2}. Adding the fluence during the plasma pulses (flux in the range 1 · 10^{26} m^{-2} s^{-1} for 1 ms [17]), the total fluence scaled up to 1.4 · 10^{26} m^{-2}. This value was matched for other steady-state exposures, both in H and in He. During the He exposures of samples He_1 and He_2, 10% (gas flow) of H was added to the plasma in order to improve the stability (reduce the arc voltage) and cleanliness of the plasma source (prevent the impurity deposition on the sample). However, in both cases (pure He and He+10%H), we observed the same cracking pattern on the samples, which indicated that the presence of H in the plasma did not change He results. Previous works have shown that in fact He suppresses D retention in W [27, 28] and similar surface modifications were observed for pure He and mixed D/He plasmas [8].

The mass of the W samples was measured before and after exposure to the plasma and the observed changes were negligible, indicating no net erosion. Surface morphology changes were investigated with a scanning electron microscope (SEM) while changes in the near-surface region were investigated by cross-sectioning the samples using a focused ion beam (FIB). Roughness measurements (R_a defined as the root-mean-square deviation of the profile height from the mean level) were performed using a DEKTAK stylus profilometer. Exposure conditions and roughness after irradiation are given in table 1.

W samples were also exposed to simultaneous plasma discharges and a high power fibre-coupled Nd: YAG laser (LASAG FLS 352-302) with pulse duration of 1 ms and repetition rate of 10 Hz. The temporal shape of the laser pulse was nearly square waveform and the laser beam could be approximated to a Gaussian profile (FWHM $\approx$ 1 mm). More details of the laser setup can be found in [29]. The same W grade was supplied by Plansee AG and cut in discs with 1 mm thickness from a rolled W rod of 99.97% purity. After polishing, samples were thoroughly rinsed with water, and as a final step ultrasonically cleaned in an acetone and ethanol. They were exposed to He plasma fluences of up to 10^{26} m^{-2} with ion energy of 18 eV, while simultaneously being exposed to laser pulses of 80 MW m^{-2} (sample 1) and 480 MW m^{-2} (sample 2). The total number of laser pulses was ~3000 during 500 s of plasma exposure time. The base temperature was kept at 1000 K.

3. Results

3.1. Pulsed plasma source

The results of pure H plasma exposure will be discussed first as they will serve as references to discuss the effect of He. Two series of experiments were performed with different base temperatures (~700–800 K and 1000–1100 K—determined

Table 1. Summary of the exposure conditions of W samples at pilot-PSI.

Sample name	Gas mixture	Fluence (m^{-2})	Base T (K)	Delta T (K)	Number of transient pulses	Energy density $(MJ\,m^{-2})$	R_a after exposure (nm)
He_1	He	7.7×10^{25}	850	320 ± 14	660	$0.277 \pm 8 \times 10^{-3}$	37
He_2	He	7.6×10^{25}	1070	240 ± 8	560	$0.234 \pm 6 \times 10^{-3}$	44
H_1	H	3.6×10^{25}	800	570 ± 25	660	$0.310 \pm 18 \times 10^{-3}$	118
H_2	H	3.2×10^{25}	1120	720 ± 62	560	$0.439 \pm 13 \times 10^{-3}$	120
H_3	H	2.9×10^{25}	670	370 ± 48	960	$0.185 \pm 28 \times 10^{-3}$	38
H_4	H	3.1×10^{25}	980	490 ± 51	960	$0.233 \pm 24 \times 10^{-3}$	207
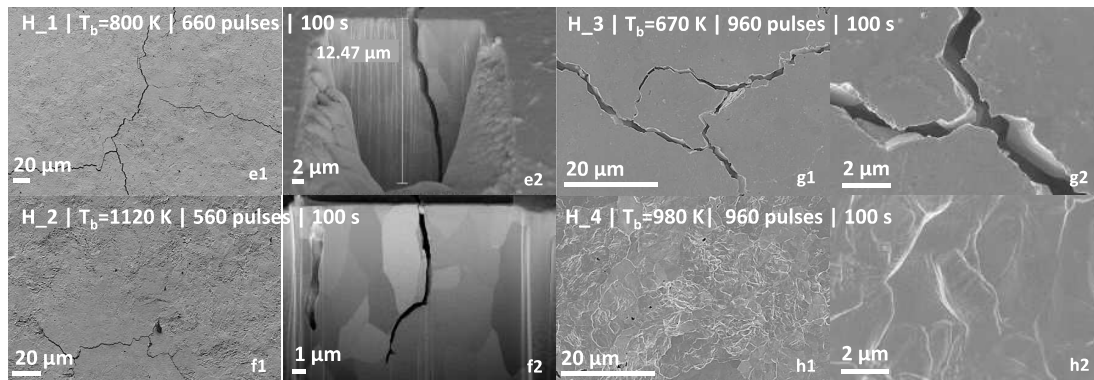
Figure 3. W samples exposed to H plasma for 100 s at 800 K and 660 pulses (*e1*) and (*e2*), 1120 K and 560 pulses (*f1*) and (*f2*), 670 K and 960 pulses (*g1*) and (*g2*), 980 K and 960 pulses (*h1*) and (*h2*).

by the inter-ELM heat flux density) and different transient peak heat fluxes (~200–300 MW m^{-2} and >500 MW m^{-2}). It should be noted that these experiments are challenging and a perfect match of either the base temperature or the transient heat flux is difficult so that some variation between the H and He exposures is present. In addition, due to a technical error, the number of transient pulses could not be kept constant between the two series of experiments. This will however not affect the main conclusions of the study.

For the high transient heat flux case (samples H_1 and H_2 in table 1), cracking is observed for both base temperatures studied (figure 3). At a base surface temperature $T_b = 800$ K, large cracks, up to 2 μm wide and more than 28 μm deep, were found. At higher temperature (1120 K), similar sparse cracks were formed but they propagated to smaller depths, typically up to ~11 μm. At lower energy density, one large crack was found at 670 K (*g1*) and (*g2*), easily visible to the bare eye. At higher temperature 980 K (*h1*) and (*h2*) the surface of the sample was considerably roughened but no cracks were observed. Except for H_3 (lower base temperature), all the other samples suffered an increase of the surface roughness. During the repetitive transient loading, the large temperature gradient (along the plasma-exposed surface) and the short time between pulses does not allow for a complete release of the compressive stresses, leading to plastic deformation [30]. For reference, samples were also exposed to a steady state H plasma (no ELM-like pulses) at 770 K and 1070 K and as expected no cracking or other modifications were observed.

Similar experiments were repeated with He plasmas. Plasma exposure for 100 s at 850 K (figures 4(*a1*)–(*a3*)) and 1070 K (figures 4(*b1*)–(*b3*)) with 660 and 560 plasma pulses respectively, resulted in the formation of a fine crack network in case of higher temperature (1070 K), while at lower temperature (850 K) cracks were more sparse. The cracking pattern formed in this case was different from the H exposures in terms of surface coverage and crack width (<200 nm). Very fine cracks were formed covering the entire exposed surface of the sample and propagating deeper than 2 μm. No surface roughening occurred after plasma exposure. A thin porous layer of about 78–130 nm was formed on the surface, which, based on the EDX analysis, was formed due to the impurity deposition during plasma operation. The elemental composition of the layer indicated that the impurities mainly originated from the erosion of the boron nitride insulators mounted between the cascaded plates of the plasma source. The fine cracks which were formed at higher temperature were about 100 nm wide and spread several μm in depth, with no clear indication of an along-the grain-boundary propagation.

Differently from the similar He exposure at high temperature, where the cracking network covered the whole exposed area with fine cracks, in the H case they were sparse and more localized (all samples except H_4). It is interesting to note that for $T \sim 1000$ K, and for similar pulse number and energy density, roughening was observed in the H plasma case while no roughening but surface cracking was observed for the He case. This suggests that the surface remained brittle during the He exposure despite the elevated temperature. He embrittlement of metals following neutron irradiation (and He production within the material) is for example discussed in [31, 32]. The present results indicate that He embrittlement can occur from
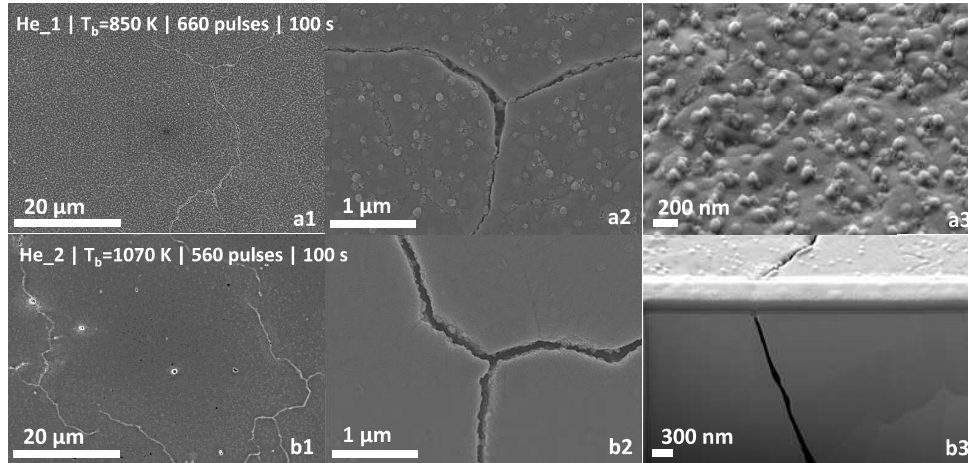
Figure 4. W samples exposed to He plasma for 100 s at 850 K (*a1*)–(*a3*) and 1070 K (*b1*)–(*b3*) at 660 and 560 plasma pulses respectively ((*b3*) is cross-sectional view).

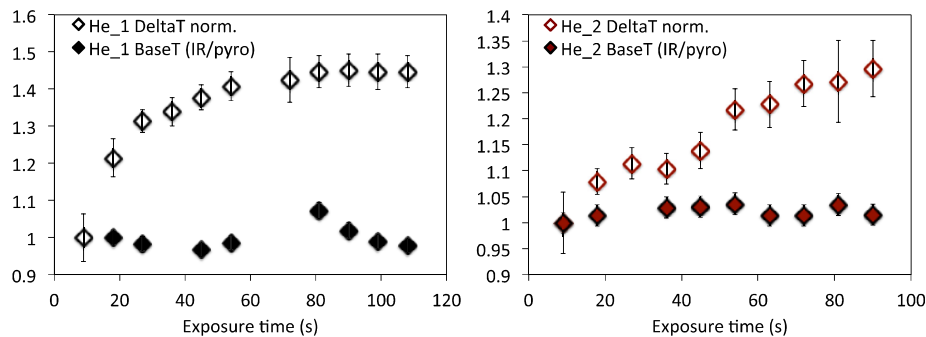**Figure 5.** ΔT is normalized over the first pulses and plotted versus exposure time for samples exposed to He transients: He_1 (850 K, 660 pulses) and He_2 (1070 K, 560 pulses). Base T is the ratio between the IR and pyrometer values at every time-step.

plasma exposure, despite the narrow implantation range, and can affect the thermal shock behavior of the material.

As stated in the experimental section, an IR camera and a pyrometer (spot size of 2 mm [24]) were used to measure the surface temperature during exposure. In figures 5 and 6, the time dependence of ΔT_{ELM} (temperature increase caused by the ELM-like plasma pulse), normalized over the first set of pulses, is plotted for He exposed samples. Each data point represents an average of ΔT over a number of pulses (~50–140) per plasma discharge. In addition, the ratio between the base temperatures measured by the IR camera and pyrometer are also plotted. The good agreement between the IR and pyrometer temperatures, and the fact the ratio of both measurements does not evolve over the course of the experiment indicates that the surface emissivity remains constant during the experiments. During He pulsed plasma exposure, ΔT increased with exposure time by 30–45% compared to the first discharge. Given that the surface emissivity remains constant, the increase of ΔT is attributed to changes in the surface thermal conductivity caused by the energy deposition during the pulsed plasma exposure.

In contrast, for the H exposures (figure 6) there is no clear dependence of the ELM-induced temperature rise with exposure duration, except for the low exposure temperatures (H_3, H_1) where the ΔT increased by about 30% compared to the

first plasma pulses. In addition, the IR camera reading of the base temperature deviated from the pyrometer values, indicating changes in the emissivity possibly due to the progressive surface roughening.

3.2. Laser heating

In order to better understand the variations of ΔT, additional experiments were performed using a pulsed laser to simulate transient heat loads in He plasma. The unique advantage of using the pulsed plasma source in this study is its capacity to generate transient heat and particle loads simultaneously. However, the use of a laser provides more reproducible conditions and allows for larger pulse numbers. Previous studies of the effect of laser-induced transient heat loads during H plasma exposure showed an increase in ΔT_{ELM} as a function of exposure time and incident heat flux. A deterioration of the power handling capability of damaged W with the number of pulses, as determined by the changes in the absorbance of the laser light, was reported [29].

W samples were exposed to He plasma discharges while simultaneously being exposed to ~3000 laser pulses of 80 MW m^{-2} (sample 1: $F_{\text{HF}} = 2.5$ MJ m^{-2} s$^{-1/2}$) and 480 MW m^{-2} (sample 2: $F_{\text{HF}} = 15.3$ MJ m^{-2} s$^{-1/2}$) energy per pulse at 1000 K base temperature. The heat load parameter
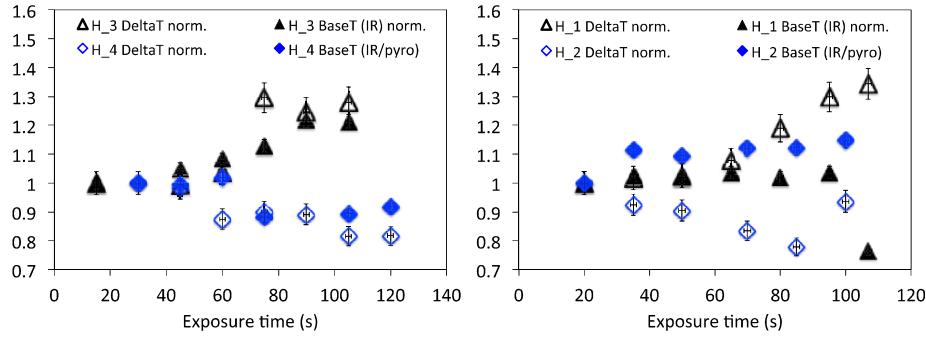
Figure 6. ΔT is normalized over the first pulses and plotted versus exposure time for all samples exposed to H transients. Base T is the ratio between the IR and pyrometer values (at every time-step) or IR only when the pyrometer data are not available.
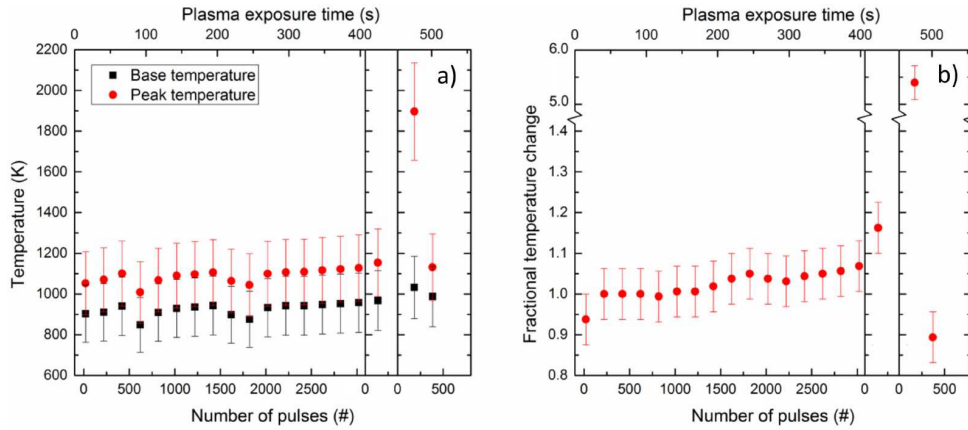

Figure 7. Sample 1 (low power ELM, $T_b = 1000$ K): (*a*) base and peak temperature are plotted as a function of time and number of laser pulses. (*b*) The fractional change in ΔT ($\Delta T = T_{peak} - T_{base}$). The sections on the far right of each graph show the results from the second and third laser position (# of pulses resets to 0) on the same target (plasma exposure time continues) for direct comparison. At ~480 s, the laser was realigned and a shot of 12 J laser energy instead of 2 J was performed to investigate the effect on subsequent exposure to another 2 J shot at ~500 s.

was calculated using the laser spot size of 2.78 mm^2 (A), laser pulse duration 1 ms (t), LASAG system transmission 51% and input energy 12 J and 2 J (E) for the high and low heat load respectively ($F_{HF} = E/(At^{0.5})$).

Figure 7(*a*) shows the base and peak temperature for sample 1 (low power ELM, $T_b = 1000$ K). After 400 s of exposure, the laser was realigned to a new position where one shot was performed. Since the plasma beam diameter was much larger than the laser spot, this allowed the effect of plasma exposure only to be assessed. After 450 s of plasma exposure, another realignment took place and a shot with high laser energy (15.3 MJ m^{-2} s$^{-1/2}$) was performed, followed by another shot with low laser energy (2.5 MJ m^{-2} s$^{-1/2}$) at the same location. Figure 7(*b*) shows the fractional change of ΔT ($\Delta T = T_{peak} - T_{base}$) corresponding to the temperatures plotted in figure 7(*a*). Note that ΔT only slightly increased during the experiment, and was slightly higher after the first laser realignment. Note the break in the fractional temperature change axis of the graph, as ΔT is a factor 5.4 higher during the high laser power shot. The low energy shot following the high-energy shot produced a noticeably lower ΔT than the low energy laser shot at 420 s.

Similarly, in figure 8(*a*) the base and peak temperature are plotted for sample 2 (high power ELM, $T_b = 1000$ K) while in figure 8(*b*) is shown the fractional change in ΔT as the experiment progresses. After about 500 s of plasma exposure, the laser was again realigned to a different position on the same target. The results again showed that on the new spot the peak temperature returned to its initial value of ~1800 K. The fractional change in ΔT showed the same behavior (figure 8(*b*)). At around 175 s of plasma exposure, a break of 25 s is present in the upper axis of figure 8(*b*) due to the LASAG system failing while plasma exposure continued. Consequently, as no laser pulses were fired, no peak temperature was recorded for that shot. Interestingly, comparing figures 5(*b*) and 8(*b*), the fractional temperature change increased more rapidly in the first case which may indicate faster degrading of the material due to the presence of higher particle flux, in addition to the heat flux.

As shown in both cases (figures 7 and 8), the ΔT measured on the new spot is almost identical to that measured at the beginning of the plasma exposure on the pristine surface. This indicates that the rise in ΔT was caused by surface damage and roughening (no W melting occurred), both of which were observed in SEM images. Laser pulses caused roughening of
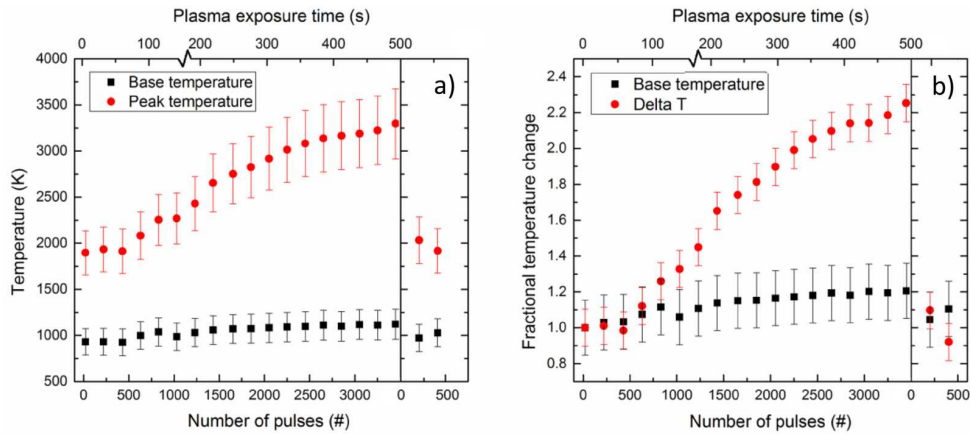
Figure 8. Sample 2 (high power ELM, $T_b = 1000$ K): (*a*) base and peak temperature plotted as a function of time and number of laser pulses. (*b*) The fractional change in ΔT and base temperature. The sections on the far right of each graph show results from the new laser position (# of pulses resets to 0 after the laser was realigned) on the same target (plasma exposure time continues) for direct comparison. Both graphs show the base and peak temperatures of the new spot similar to the values at the beginning of the plasma exposure. The break from 175 to 200 s is caused by a plasma shot where the LASAG laser failed.
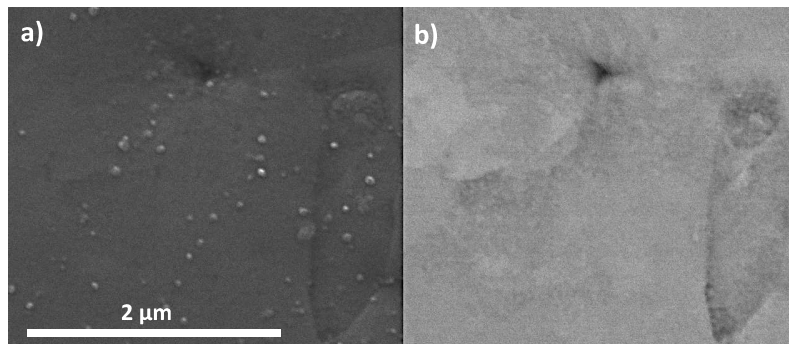

Figure 9. SEM images of sample 1 at the position where the laser struck the sample, magnified ~43 000× (*a*) SEM image, (*b*) backscattering emission.

the W surface and the early onset of the damage, where individual grains were displaced due to thermal cycling induced stress while pulsed plasma source caused more severe cracking on W. The low power ELM simulations did not cause visible damage on W. As a result, no surface morphology changes were observed by SEM. High magnification (~43 000×) of Sample 1 is shown in figure 9, SEM is on the left and BSE-mode (backscattering emission) is on the right.

Figure 10(*a*) shows the SEM imaging results for Sample 2 (high power ELM, $T_{base} = 1000$ K). The image shown is a combination of the regular electron microscopy and the backscatter emission (BSE) signal. In this case, BSE mainly provides additional topological insight in the surface. In figure 10(*b*) is shown the image of the second laser spot, which has been exposed to 400 laser pulses after first being exposed to a He-plasma fluence of about 10^{26} m^{-2} at a base temperature of ~1000 K.

The damage and roughness resulted in decreased power handling and increased absorptivity of the laser light respectively, both of which can account for rises in ΔT. However, an analysis of the IR images of sample 2 (high laser power) indicated the emissivity at the laser spot increased by ~18% after ~1000 laser shots as a result of surface roughening. In the

meantime, ΔT increased by a factor 2 at least, so the observed changes cannot be attributed solely to changes in optical properties, which contribute only to part of the observed temperature increase.

With the laser position changed, the observation of increased ΔT in comparison to the measurement series spanning 0–400 s of plasma exposure could indicate that the He-bubble infused top layer grows faster in the absence of laser loading. This suggests a possibility that pulsed heatloads anneal the (sub) surface of W from He-induced effects, a hypothesis which is investigated and tested. This would also explain the decrease in ΔT at 500 s (figure 8), as the preceding pulse with high-power ELMs would have annealed the surface completely.

Figure 11 shows the evolution of ΔT within two separate high power series of laser pulses on areas of W exposed to ~500 s of He-plasma only (without ELM transients). At the beginning of the shot an exponential decay of ΔT is observed, indicating that the top layer of the sample is altered within the first ~80 laser pulses. The measured ΔT then reached a steady-state value. It is known [33] that the formation of He bubbles in the near-surface region leads to a strong decrease in the surface thermal conductivity. It is therefore interesting
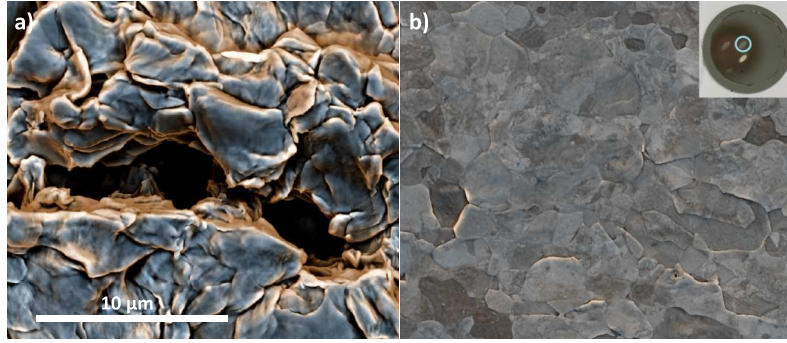
Figure 10. (*a*) SEM image of an area on the tungsten sample exposed to simultaneous helium plasma and >3000 high-energy ELM-like pulses at base temperature ~1000 K. (*b*) SEM image of the second laser spot, exposed to 400 high power laser pulses after a He-plasma fluence of about $1.0 * 10^{26}$ m^{-2} at a base temperature of ~1000 K.
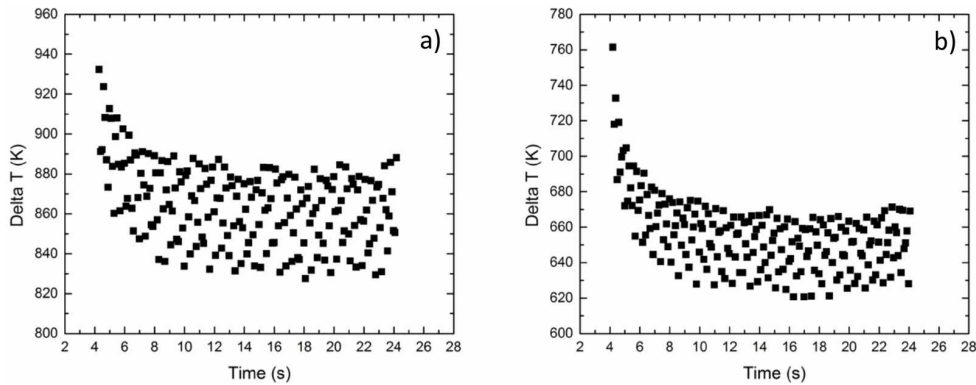

Figure 11. Recorded ΔT values for 200 high power laser pulses performed on W exposed to ~500 s of He plasma. (*a*) (Sample 1): Individual measurements within the data point at $t = 480$ s. (*b*) (Sample 2): Individual measurements within the data point at $t = 520$ s. In the first 10 s (~80 pulses) an exponential decay in ΔT is observed in both cases, with a temperature difference of 50–140 K.

to see whether the observed effect could be attributed to the annealing of He bubbles caused by the laser irradiation.

Pulsed laser loading experiments performed by van Eden on fuzzy W at similar plasma fluence ($9.97 * 10^{25}$ He$^+$ m^{-2} at ~1400 K) and heat load ($F_{HF} = 16.2$ MJ m^{-2} s$^{-1/2}$) showed similar behavior in ΔT, where ΔT decreased by a factor 0.9 after 100 pulses [29]. The interesting notion here is that van Eden's experiments on fuzzy W show behavior similar to the non-fuzzy W in this study. As fuzzy W is also rich with subsurface He bubbles, the decay in both cases may be attributed to high power ELMs annealing the bubbles from the subsurface.

The expected small thickness of the region where He bubbles form effectively means that a temperature gradient across this layer during a laser pulse can be assumed absent. From the heat transfer coefficient of W, ΔT for the subsurface layer can be calculated through formula (1), where C is the heat flux, k the thermal conductivity and d the thickness of the layer.

$$\Delta T = \frac{Cd}{k} \qquad (1)$$

From previous studies [34] it is known that He bubbles form in a narrow region of thickness ~30–50 nm. Assuming $d = 50$ nm, with $C = 0.5$ GW m^{-2}, $k = 150$ W m^{-1} K^{-1}, and with $\Delta T = 50$ as shown in figure 11, a reduction of the thermal conductivity by a factor 300 would be consistent with the 50 K difference between the He-modified and annealed surface.

Interestingly, this is consistent with the measurements from [33]. It confirms that the above-mentioned change in ΔT (figure 11) is in large part due to damage of the target caused by pulsed plasma exposure and that He-induced bubbles only contribute to a very small fraction of the observed modified thermal behavior of the target.

4. Conclusions

Surface morphology and thermal conductivity changes after exposure of W samples to He steady state and transient plasmas were investigated and compared with those caused by similar exposures in H. Exposure to He plasma pulses caused the formation of a fine cracking network on W samples which occurred at a higher density and smaller depths compared to H pulsed plasma irradiation. The peak temperature, after exposure to pulsed plasmas, increased by a factor of ~1.3 (in H) and ~1.3–1.45 (in He) compared to the first plasma pulses, indicating an alteration of the thermal properties of the target. Cracking of the He-exposed surface occurred even at ~1000 K base temperature while strong roughening caused by plastic deformation was observed for the H exposure. This suggests a He-induced embrittlement of the surface and an increased sensitivity to cracking.

In addition, simultaneous He plasma and laser pulses exposure of W samples were performed. The transient-induced

temperature excursion increased by a factor of ~2.3 during the exposure at 1000 K base temperature and high laser pulse power (480 MW m^{-2}). Investigation of the thermal response of a W surface after the plasma exposure showed a recovery of the surface thermal properties after ~80 laser pulses at energy density 0.5 MJ m^{-2} indicating that the surface modifications might anneal out by the laser irradiation. The present results suggest that the observed changes in ΔT are caused in large part by surface damage/modification occurring during transient loading and only to a very small extent by He-induced morphology changes. The fractional temperature change increased more rapidly in the pulsed plasma source case, which may indicate faster degrading of the material due to the presence of higher particle flux, in addition to the heat flux.

Based on these findings, pure He plasma operations in ITER are likely to lead to W surface cracking at lower transient energy densities than would occur in H plasma. However, since the cracking threshold is in any case low at high pulse numbers [35], it is likely that cracking would occur anyway given the high expected ELM number in ITER [22]. From these results and previous work, it seems clear that, either in the He or D/T phases, ELM-induced cracking and roughening of W surfaces are difficult to avoid if full ELM-suppression is not achieved. To date, however, it is not totally clear how ELM-induced surface damage affects the long-term behavior of the plasma-facing material in terms of power handling and impurity release. Therefore, systematic investigations of the effect of long-term stationary and transient plasma exposure need to be performed to quantify the level of tolerable surface damage in ITER.

Acknowledgments

ORCID iDs

T.W. Morgan ⓘ https://orcid.org/0000-0002-5066-015X
M. Rasinski ⓘ https://orcid.org/0000-0001-6277-4421

References

[1] Loarte A. 2007 Progress in the ITER physics basis chapter 4: power and particle control *Nucl. Fusion* **47** S203–63
[2] Pitts R. 2013 A full tungsten divertor for ITER: physics issues and design status *J. Nucl. Mater.* **438** S48–56
[3] Jia Y. 2015 Thermal shock behaviour of blisters on W surface during combined steady-state/pulsed plasma loading *Nucl. Fusion* **55** 113015
[4] Kajita S. 2011 TEM observation of the growth process of helium nanobubbles on tungsten: Nanostructure formation mechanism *J. Nucl. Mater.* **418** 152–8
[5] Fiflis P. 2015 Direct time-resolved observation of tungsten nanostructured growth due to helium plasma exposure *Nucl. Fusion* **55** 033020
[6] Kajita S. 2007 Sub-ms laser pulse irradiation on tungsten target damaged by exposure to helium plasma *Nucl. Fusion* **49** 1358–66
[7] Kajita S. 2009 Formation process of tungsten nanostructure by the exposure to helium plasma under fusion relevant plasma conditions *Nucl. Fusion* **49** 095005
[8] Miyamoto M. 2011 Microscopic damage of tungsten exposed to deuterium–helium mixture plasma in PISCES and its impacts on retention property *J. Nucl. Mater.* **415** S657–60
[9] Rudakov D. 2016 Exposures of tungsten nanostructures to divertor plasmas in DIII-D *Phys. Scr.* **T167** 014055
[10] De Temmerman G. 2013 Helium effects on tungsten under fusion-relevant plasma loading conditions *J. Nucl. Mater.* **438** S78–83
[11] Gunn J.P. 2017 Surface heat loads on the ITER divertor vertical targets, *Nucl. Fusion* **57** 046025
[12] Garkusha I. 2012 Transient plasma loads to the ITER divertor surfaces: simulation experiments with QSPA Kh-50 *Nukleonika* **57** 167–70 (http://nukleonika.pl/www/back/full/vol57_2012/v57n2p167f.pdf)
[13] Yu J. 2014 ITER-relevant transient heat loads on tungsten exposed to plasma and beryllium *Phys. Scr.* **T159** 014036
[14] Takamura S. and Uesugi Y. 2015 Coupled interactions between tungsten surfaces and transient high-heat-flux deuterium plasmas *Nucl. Fusion* **55** 033003
[15] Suslova A. 2015 Material ejection and surface morphology changes during transient heat loading of tungsten as plasma-facing component in fusion devices *Nucl. Fusion* **55** 033007
[16] Poznyak I. 2016 Properties of tungsten vapor plasma formed at conditions relevant to transient events in ITER at plasma gun facility MK-200UG *AIP Conf. Proc.* **1771** 060006
[17] De Temmerman G. 2011 ELM simulation experiments on pilot-PSI using simultaneous high flux plasma and transient heat/particle source *Nucl. Fusion* **51** 073008
[18] Hirai T. 2016 Use of tungsten material for the ITER divertor *Nucl. Mater. Energy* **9** 616–22
[19] Morgan T. 2014 A high-repetition rate edge localised mode replication system for the magnum-PSI and pilot-PSI linear devices *Plasma Phys. Control. Fusion* **56** 095004
[20] van der Meiden H. 2012 Advanced Thomson scattering system for high-flux linear plasma generator *Rev. Sci. Instrum.* **83** 123505
[21] LaBombard B. 1989 Presheath profiles in simulated tokamak edge plasmas *J. Nucl. Mater.* **162–4** 314–21
[22] Loarte A. 2014 Progress on the application of ELM control schemes to ITER scenarios from the non-active phase to DT operation *Nucl. Fusion* **54** 033007
[23] Pacher H. 2011 Modelling of the ITER reference divertor plasma *J. Nucl. Mater.* **415** S492–6
[24] van den Berg M. 2013 Thermographic determination of the sheath heat transmission coefficient in a high density plasma *J. Nucl. Mater.* **438** S431–4
[25] Hermann A. 1995 Energy flux to the ASDEX-upgrade diverter plates determined by thermography and calorimetry *Plasma Phys. Control. Fusion* **37** 17–29
[26] Eich T. 2007 ELM resolved energy distribution studies in the JET MKII gas-box divertor using infrared thermography *Plasma Phys. Control. Fusion* **49** 573–604
[27] Baldwin M. 2011 Effect of He on D retention in W exposed to low-energy, high-fluence (D, He, Ar) mixture plasmas *Nucl. Fusion* **51** 103021

[28] Miyamoto M. 2009 Observations of suppressed retention and blistering for tungsten exposed to deuterium–helium mixture plasmas *Nucl. Fusion* **49** 065035

[29] van Eden G. 2014 The effect of high-flux H plasma exposure with simultaneous transient heat loads on tungsten surface damage and power handling *Nucl. Fusion* **54** 123010

[30] Loewenhoff T. 2011 Evolution of tungsten degradation under combined high cycle edge-localized mode and steady-state heat loads *Phys. Scr.* **T145** 014057

[31] Gilbert M. 2013 Neutron-induced dpa, transmutations, gas production, and helium embrittlement of fusion materials *J. Nucl. Mater.* **442** S755–60

[32] Baskes M. 1986 Recent advances in understanding helium embrittlement in metals *MRS Bull.* **11** 14–8

[33] Dechaumphai E. 2014 Near-surface thermal characterization of plasma facing components using the 3-omega method *J. Nucl. Mater.* **455** 56–60

[34] Thompson M. 2015 Probing helium nano-bubble formation in tungsten with grazing incidence small angle x-ray scattering *Nucl. Fusion* **55** 042001

[35] Loewenhoff T. 2015 Impact of combined transient plasma/heat loads on tungsten performance below and above recrystallization temperature *Nucl. Fusion* **55** 123004